Published in final edited form as:
Dev Cell. 2006 November ; 11(5): 629–640. doi:10.1016/j.devcel.2006.09.002.

Myosin-1c Couples Assembling Actin to Membranes to Drive Compensatory Endocytosis

Anna M. Sokac[1,2,4], **Cataldo Schietroma**[3], **Cameron B. Gundersen**[3], and **William M. Bement**[1,2,*]

[1]Program in Cellular and Molecular Biology, University of Wisconsin-Madison, Madison, Wisconsin 53706

[2]Department of Zoology, University of Wisconsin-Madison, Madison, Wisconsin 53706

[3]Department of Molecular and Medical Pharmacology, David Geffen UCLA School of Medicine, University of California, Los Angeles, Los Angeles, California 90095

Summary

Compensatory endocytosis follows regulated exocytosis in cells ranging from eggs to neurons, but the means by which it is accomplished are unclear. In *Xenopus* eggs, compensatory endocytosis is driven by dynamic coats of assembling actin that surround and compress exocytosing cortical granules (CGs). We have identified *Xenopus laevis* myosin-1c (*Xl*Myo1c) as a myosin that is upregulated by polyadenylation during meiotic maturation, the developmental interval that prepares eggs for fertilization and regulated CG exocytosis. Upon calcium-induced exocytosis, *Xl*Myo1c is recruited to exocytosing CG membranes where actin coats then assemble. When *Xl*Myo1c function is disrupted, actin coats assemble, but dynamic actin filaments are uncoupled from the exocytosing CG membranes such that coats do not compress, and compensatory endocytosis fails. Remarkably, there is also an increase in polymerized actin at membranes throughout the cell. We conclude that *Xl*Myo1c couples polymerizing actin to membranes and so mediates force production during compensatory endocytosis.

Introduction

Dynamic interactions between the actin cytoskeleton and cellular membranes are required for essential processes including endo- and exocytosis, cell locomotion, cell division, and vesicle motility. Force production is inherent to these processes, and intense effort has been expended to identify the means by which the actin cytoskeleton exerts force on membrane compartments. Two general mechanisms have been described: force exerted on membranes by actin assembly, exemplified by actin polymerization at the plasma membrane (PM) of the leading edge of crawling cells (Welch and Mullins, 2002), and force exerted via myosin-

*Correspondence: wmbement@wisc.edu.
[4]Present address: Department of Molecular Biology, Princeton University, Washington Road, Princeton, NJ 08544.

Supplemental Data
Supplemental Data include ten movies and corresponding movie descriptions and are available at http://www.developmentalcell.com/cgi/content/full/11/5/629/DC1/.

Accession Numbers
The myosin sequences obtained in this study have been entered into GenBank with the following accession numbers: *Xl*Myo1b, EF026166; *Xl*Myo1c, EF026164; *Xl*Myo1d, EF026167; *Xl*Myo1e, EF026163; *Xl*Myo1f, EF026168; *Xl*Myo2a, EF026169; *Xl*Myo3, EF026170; *Xl*Myo6, EF026171; *Xl*Myo9a, EF026172; *Xl*Myo9b, EF026173; *Xl*Myo10, EF026174; *Xl*Myo18, EF026165.

based translocation of actin-associated membranes, exemplified by myosin-2-powered PM ingression during cytokinesis (Yumura and Uyeda, 2003).

The unconventional myosins (classes 1 and 3–18) have attracted considerable attention as potential motors for actin-dependent force production on membranes because these motors typically bind membranes in vitro and associate with membrane compartments in vivo (Sokac and Bement, 2000). Furthermore, disrupting the function of specific unconventional myosins can alter the distribution or motility of their associated membrane compartments (e.g., Doberstein et al., 1993).

Myosins-1 are the most abundant and diverse class of unconventional myosins. In vertebrates, they are represented by four distinct subclasses (Coluccio, 1997) and have been implicated in endocytosis (Soldati, 2003) and exocytosis (Bose et al., 2002). But how myosins-1 contribute to these processes in vertebrates is unknown. While the textbook model of unconventional myosins as membrane transport motors predicts that they carry endosomes and secretory compartments along actin filaments (F-actin), recent work in budding yeast suggests that myosins-1 can participate in endocytosis both by promoting actin assembly and by transport of F-actin (Sun et al., 2006).

To understand the roles played by myosins-1 in vertebrate cells, we have analyzed their expression and function during activation of *Xenopus laevis* eggs. Egg activation in *Xenopus* and other vertebrate and invertebrate species is triggered at fertilization by an increase in intracellular free calcium ($[Ca^{2+}]_i$) and entails a series of rapid, essential events that depend on F-actin/membrane interactions. These include cortical contraction, required for pronuclear fusion (Elinson, 1977), cortical granule (CG) exocytosis, required for the slow block to polyspermy (Wolf, 1974), assembly of dynamic actin coats around exocytosing CGs, required for compensatory endocytosis (Sokac et al., 2003), and assembly of actin comets (Taunton et al., 2000). The *Xenopus* system is ideal for analysis of myosin function during egg activation in that the events of fertilization can be mimicked by artificial elevation of $[Ca^{2+}]_i$, exogenous constructs can be expressed by microinjection of mRNA, and four-dimensional (4D) imaging permits detailed analysis of cytoskeletal dynamics with exceptional clarity (Sokac et al., 2003).

Using an expression screen, we identify *Xenopus* Myosin-1c (*Xl*Myo1c; formerly known as myosin-1β or myr 2) as a myosin specifically upregulated by polyadenylation during meiotic maturation, the developmental interval that prepares oocytes for fertilization. We show that *Xl*Myo1c is rapidly recruited to exocytosing CGs and that disruption of *Xl*Myo1c function perturbs several events of egg activation, including compensatory endocytosis. Surprisingly, the primary phenotype underlying these egg activation defects is misdirected actin assembly whereby dynamic actin is uncoupled from the appropriate membrane compartments. Thus, rather than acting as a transporter, *Xl*Myo1c instead links polymerizing actin to membranes such that actin assembly exerts force on the membranes.

Results

Identification and Expression of *Xenopus* Myosins

Xenopus oogenesis proceeds through six defined growth stages, followed by progesterone-triggered meiotic maturation to convert the stage 6 oocyte into the fertilizable egg, followed by calcium-dependent egg activation at fertilization. Oogenesis occurs over the course of months, meiotic maturation takes 3–12 hr, and activation commences within seconds of sperm-induced calcium elevation. To identify myosins that might participate in *Xenopus* egg activation, we screened by degenerate polymerase chain reaction (PCR) (Bement et al., 1994) and amplified small fragments of 12 different myosins, representing seven myosin

classes (see Experimental Procedures). Six myosins (Myosin-1c, 1e, 2a, 3, 9b, and 10) were selected for amplification of larger fragments by using exact-match primers paired to downstream degenerate primers. The fragments thus obtained, as well as γ-actin, were used to probe poly(A)$^+$ RNA blots of stage 1–6 oocytes as well as meiotically mature eggs. Most myosins and γ-actin showed high expression in early oogenesis (stages 1–3), decreasing expression up to stage 6, and a sharp decline during meiotic maturation (Figure 1A). This decrease presumably reflects the de-adenylation of most mRNAs during meiotic maturation (Liu and Smith, 1994). The sole exception to this pattern was *Xenopus* Myosin-1c (*Xl*Myo1c): while the general decrease during oogenesis was observed, poly(A)$^+$ levels increased during meiotic maturation such that eggs have more *Xl*Myo1c poly(A)$^+$ RNA than stage 6 oocytes (Figure 1A).

*Xl*Myo1c Is Upregulated by Polyadenlyation during Meiotic Maturation

The upregulation of *Xl*Myo1c poly(A)$^+$ RNA during meiotic maturation could result from selective polyadenylation, an exciting possibility in that such regulation is normally restricted to mRNAs encoding proteins required for meiotic maturation and early development (Sheets et al., 1994; Robbie et al., 1995). To test this directly, both total RNA and poly(A)$^+$ RNA were isolated from stage 6 oocytes and meiotically mature eggs and then probed for *Xl*Myo1c, γ-actin, or *Xl*Myo2a. There was no apparent change in the levels of total RNA between stage 6 oocytes and meiotically mature eggs for *Xl*Myo2a, *Xl*Myo1c, or γ-actin (Figure 1B). In contrast, both *Xl*Myo2a and γ-actin poly(A)$^+$ RNA levels decreased upon meiotic maturation, while *Xl*Myo1c poly(A)$^+$ RNA levels increased, confirming that the latter is selectively polyadenylated. Immunoblotting showed that *Xl*Myo1c protein levels concomitantly increased during meiotic maturation, but *Xl*Myo2a and γ-actin levels did not (Figure 1C).

The complete *Xl*Myo1c coding sequence was obtained by rapid amplification of cDNA ends (RACE) (Figure 1D). Its deduced primary structure predicts all of the expected features of a myosin-1c: an N-terminal “head” with the actin and ATP-binding motor domain (Reizes et al., 1994), a “neck” comprised of three IQ motifs that bind calmodulin (Zhu et al., 1998; Tang et al., 2002), and a highly basic (pI = 10.4) C-terminal “tail” that directs membrane interaction (Tang et al., 2002) (Figures 1D and 1E). In addition, two alternative 3′ untranslated regions (UTRs) were identified, one of which contains a cytoplasmic polyadenylation element (Figure 1F) that could account for the polyadenylation of *Xl*Myo1c during meiotic maturation (Gray and Wickens, 1998).

*Xl*Myo1c Localizes to the PM and to Exocytosing CGs upon Egg Activation

To characterize the subcellular distribution of *Xl*Myo1c, an eGFP-*Xl*Myo1c fusion was generated and expressed in oocytes and eggs. In both oocytes and eggs, confocal analysis of fixed samples showed that eGFP-*Xl*Myo1c localizes to the PM, coincident with cortical F-actin (Figure 2A). After calcium ionophore-induced activation, eGFP-*Xl*Myo1c moved to some CGs, as revealed by eGFP-*Xl*Myo1c on spherical compartments of ~1–3 μm diameter immediately beneath the PM (Figures 2A and 2B). These CGs were also encased by coats of F-actin, which only form around exocytosing CGs (Sokac et al., 2003). Z views of prick-activated eggs indicated that *Xl*Myo1c was recruited to exocytosing CGs before actin coats formed (Figure 2B). That is, pricking induces a wave of $[Ca^{2+}]_i$ increase and, therefore, a wave of CG exocytosis that emanates from the prick site. In regions far from the prick site, where exocytosis had just began upon fixation, CGs with *Xl*Myo1c, but not actin, were observed. However, in regions close to the prick site, where the exocytosis stimulus had been present longer, CGs were surrounded by both *Xl*Myo1c and actin. In intermediate areas, *Xl*Myo1c surrounded CGs, while actin coats tended to only partially encase these compartments (Figure 2B).

To confirm the localization results obtained from fixed samples expressing exogenous *Xl*Myo1c, two additional approaches were employed. First, the distribution of endogenous *Xl*Myo1c was assessed in activated eggs with an anti-mammalian myosin-1c antibody (Wagner et al., 1992). Consistent with the above results, endogenous *Xl*Myo1c localized to both the PM and exocytosing CGs (Figure 2C). Second, oocytes were fractionated to generate a cortical pellet comprised of the PM and CGs and a supernatant comprised of the cytoplasm and other membrane compartments (Gundersen et al., 2002). Immunoblotting showed that both exogenous and endogenous *Xl*Myo1c associated with the cortical fraction, along with markers for the PM and CGs (Figure 2D).

EGFP-*Xl*Myo1c distribution was next analyzed in living cells activated by photolysis of caged inositol-1,4,5-trisphoshpate (IP_3). Briefly, eggs expressing eGFP-*Xl*Myo1c were subjected to IP_3 uncaging in the presence of extracellular Texas red dextran (TR-dextran), which reveals CG exocytosis by filling the compartments created upon CG-PM fusion (Sokac et al., 2003). Time-lapse confocal imaging in a single optical plane revealed that eGFP-*Xl*Myo1c is rapidly recruited to exocytosing CGs (within 0.15 s ± 0.17 s of dextran; mean ± SEM) (Figures 2E and 2F; see Movie S1), whereas actin is recruited later (Sokac et al., 2003; see also below). Exocytosing CGs surrounded by eGFP-*Xl*Myo1c shrank over time, as observed in both en face views (Figure 2E) and z views (Figure 2F). To directly confirm that *Xl*Myo1c is recruited to CGs before actin, localization of both eGFP-*Xl*Myo1c and fluorescent actin were monitored simultaneously. Consistent with the above findings, *Xl*Myo1c was invariably recruited before actin (Figure 2G). We conclude that in resting eggs *Xl*Myo1c localizes to the PM, and upon egg activation *Xl*Myo1c is rapidly recruited to exocytosing CGs before actin coats assemble.

Contributions of *Xl*Myo1c Domains to Localization

Unconventional myosins are directed to their sites of localization via their tails (Sokac and Bement, 2000). Thus, isolated tail fragments have been widely used as dominant negatives for a variety of unconventional myosins including myosin-1c (Bose et al., 2002). We therefore generated a series of constructs encoding eGFP fused to either the head and IQ domains (HIQ), the IQ domains alone (IQ), the IQ domains and the tail (IQT), or the tail alone (T) and assayed their distribution in oocytes, eggs, and activated eggs (Figure 3A). In oocytes and eggs, eGFP-HIQ and eGFP-IQ were cytoplasmic, while eGFP-IQT and eGFP-T localized to the PM (data not shown). Following activation, eGFP-HIQ remained cytoplasmic, while eGFP-IQT and eGFP-T rapidly redistributed to some CGs, similar to full-length *Xl*Myo1c (Figure 3B). Interestingly, eGFP-IQ was also recruited to CG compartments after activation, although the high cytoplasmic signal made this recruitment harder to discern than that of eGFP-IQT or eGFP-T (Figure 3B). Thus, the tail is sufficient to direct the localization of *Xl*Myo1c, but the IQ domains also target to exocytosing CGs.

Disruption of *Xl*Myo1c Perturbs Cortical Contraction, CG Exocytosis, Actin Coat Compression, and Results in Unrestrained Actin Assembly

Based on the above results, the IQT construct was employed to disrupt *Xl*Myo1c function. Coexpression of IQT with GFP-HIQT displaced the latter from the PM in a concentration-dependent manner (Figures 4A and 4B), as expected if this construct competes with full-length *Xl*Myo1c for membrane binding sites. To assess the effects of IQT on the events of egg activation, oocytes were allowed to express IQT overnight, while undergoing progesterone-induced meiotic maturation. IQT had no apparent effect on meiotic maturation relative to either uninjected or HIQT-injected controls (Figures 4C and 4D), suggesting that IQT did not grossly perturb the cortical F-actin cytoskeleton, which is required for proper meiotic maturation (Gard et al., 1995). IQT did result in specific changes in cortical F-actin,

however, in that oocytes expressing IQT consistently had longer microvilli than either uninjected or HIQT-injected controls (Figure 4E).

IQT expression induced two phenotypes that were not evident until eggs were artificially activated with calcium ionophore. First, cortical contraction was strongly suppressed (Figures 4F and 4G). This effect was concentration dependent and could be rescued by coexpression of HIQT, demonstrating its specificity. Second, fertilization envelope elevation, a marker for CG exocytosis, was slower in eggs expressing IQT (Figure 4H). Again, this phenotype was both concentration dependent and rescued by HIQT coexpression.

To then examine the effects of IQT on CG exocytosis as well as constitutive exocytosis, a biochemical approach was taken (Gundersen et al., 2002). Two-day expression of IQT completely suppressed CG exocytosis in oocytes and eggs challenged with phorbol 12-myristate 13-acetate (PMA) and eggs challenged with ionophore (Figure 4I). Complete suppression of exocytosis following 2 day expression of IQT was not rescuable by HIQT coexpression, possibly because of the increased efficiency of IQT translation relative to the larger HIQT (data not shown). Nevertheless, this phenotype was specific, in that 2 day expression of IQT had no effect on constitutive exocytosis of either the PM Na^+-K^+ ATPase or syntaxin-1a (Figure 4J). Since constitutive exocytosis in *Xenopus* oocytes is actin dependent (e.g., Colman et al., 1981), these results again demonstrate that IQT expression is neither simply toxic nor causing wholesale disruption of the actin cytoskeleton.

In fact, we found that IQT expression actually promoted actin assembly. That is, treatment of *Xenopus* eggs with PMA results in small endosome propulsion via actin “comets,” structures comprised of rapidly polymerizing actin (Taunton et al., 2000). IQT increased the number of comets that formed in response to PMA treatment by more than 10-fold relative to uninjected and HIQT-injected controls, while coexpression of HIQT with IQT sharply reduced comet number (Figures 5A and 5B). Further, biochemical analysis confirmed that IQT expression elevated the level of actin associated with the cortical fraction, and this elevation was reduced by coexpression of HIQT (Figure 5C).

To provide independent support for the effects of IQT on actin assembly, cortical contraction, and CG exocytosis, antisense morpholinos were employed (Heasman et al., 2000). A morpholino complementary to the 5′UTR of *Xl*Myo1c resulted in a 59% reduction in *Xl*Myo1c protein relative to a five base mismatch control morpholino (Figure 6A). As with IQT expression, the *Xl*Myo1c morpholino suppressed cortical contraction (Figure 6B), increased the number of actin comets observed following PMA treatment (Figure 6C), and suppressed CG exocytosis (Figure 6D).

The microvilli and comet phenotypes, as well as the increased cortical actin levels, suggest that actin assembly goes unrestrained when *Xl*Myo1c is disrupted. This ectopic actin may perturb some events of egg activation, and if so, then inhibiting actin assembly should rescue the *Xl*Myo1c phenotypes. Obviously, this approach cannot be used for comet formation, cortical contraction, or actin coat assembly since these are all critically dependent on F-actin. However, it can be used to test CG exocytosis, which is actin independent in *Xenopus* oocytes and eggs (Sokac et al., 2003). Indeed, the effects of IQT on CG exocytosis were rescued by preincubating cells with cytochalasin D (Figure 6E). Thus, unrestrained actin assembly is likely a primary cause of the egg-activation defects observed following *Xl*Myo1c disruption.

*Xl*Myo1c Expression Uncouples Actin Coats from Exocytosing CG Membranes

The consequences of *Xl*Myo1c disruption were next analyzed in more detail by time-lapse confocal microscopy of eggs injected with Alexa488-globular-actin (G-actin) and either IQT or, as a control, HIQT. To ensure that exocytosis was not completely inhibited, IQT and HIQT were expressed overnight only. Following IP_3 uncaging, CGs rapidly exocytosed in HIQT-expressing cells, and became surrounded by actin coats that then compressed (Figure 7A; see Movie S2). IQT-expressing cells also underwent CG exocytosis following IP_3 uncaging. However, consistent with the fertilization envelope elevation results, exocytosis was slower than in HIQT-expressing cells, based on both the increased time elapsed between uncaging and appearance of TR-dextran (Figure 7A; see Movie S3) and the reduced speed with which dextran signal reached its peak in exocytosing CGs (HIQT 2.2 ± 0.15 s, IQT 4.2 ± 0.39 s; mean ± SEM; $p < 0.05$). Actin coats assembled around exocytosing CGs in IQT-expressing cells and appeared at least as robust as those in HIQT-expressing cells (Figure 7A). However, coats in IQT-expressing cells failed to compress over time and eventually dissipated. Furthermore, compression of exocytosing CGs was severely compromised (89.9% ± 2.8% in HIQT cells compressed to at least half their initial diameter within 1 min versus 13.9% ± 5.6% in IQT cells; $p < 0.05$). Consequently, many exocytosing CGs were not retrieved in IQT-expressing cells (Figure 7A; see Movie S3).

Cells were then analyzed by 4D imaging, which has the advantage of allowing visualization of dynamic processes that occur in the z dimension such as actin coat assembly and compression (Sokac et al., 2003). Apical views showed that in HIQT-expressing cells the dilated fusion pores of exocytosing CGs were rapidly covered over with actin (data not shown, but see Sokac et al., 2003), whereas in IQT-expressing cells, the fusion pores remained open (Figure 7B; see Movie S4). Similarly, basal views showed that actin coats in HIQT-expressing cells spread over the entire cytoplasmic surface of exocytosing CGs (Figure 7C; see Movie S6), while in IQT-expressing cells, most coats failed to fully enclose the exocytosing CGs (Figures 7B and 7C; see Movie S5). Rather, the coats started to form and extend into the cytoplasm but remained separated from exocytosing CGs and did not track closely along their surface (Figure 7C; see Movie S7). Tilt views of the underside of the PM showed actin fingers extending from the PM into the cytoplasm near exocytosingCGsin IQT-expressing cells (Figure 7D; see Movie S8). Such fingers grew and shrank but failed to completely enclose the CGs. The partially enclosed CGs were often squeezed to one side but were not compressed, even after many minutes (Figure 7D).

Z views further supported the notion that *Xl*Myo1c tethers assembling actin coats to exocytosing CGs. In HIQT-expressing cells, the coats extended rapidly down either side of exocytosing CGs, enclosed them, and compressed upward and inward (Figure 7E; see Movie S9). In contrast, in IQT-expressing cells, actin coats began to enclose exocytosing CGs and then shrank back, leaving the exocytosed CGs stranded beneath the PM (Figure 7E; see Movie S10).

Z views of dextran alone provided a potential explanation for the slowed exocytosis in IQT-expressing cells. Specifically, the necks of fusion pores in IQT-expressing cells were much narrower than in controls (Figure 7F). These results suggest that IQT expression might some-how limit dilation of fusion pores following CG-PM fusion, perhaps due to unrestrained actin assembly at the pore region either prior to or coincident with CG exocytosis.

Discussion

The most remarkable findings of this study are that a developmentally regulated myosin, *Xl*Myo1c, participates in egg activation by coupling dynamic actin to membranes and that

when the function of this myosin is disrupted, unrestrained actin assembly results. Egg activation entails the rapid onset of several processes dependent on precisely coordinated actin-membrane interactions (see Introduction). The consequences of *Xl*Myo1c disruption, thus, are numerous and severe: suppressed cortical contraction, superfluous actin comet formation, perturbed CG exocytosis, and impaired compression and retrieval of those CGs that do exocytose.

Of the above phenotypes, dissection of the last was the most informative. That is, *Xl*Myo1c normally localizes to exocytosing CGs. Following disruption of *Xl*Myo1c function, actin coats still assemble but fail to remain attached to the CG membrane. Thus, *Xl*Myo1c serves to tightly link the actin coat to the CG membrane, and this linkage is essential for CG compression and retrieval. How, exactly, might this work? While it is possible that *Xl*Myo1c functions by myosin-based contraction in the classic bipolar filament sense, it is predicted to be mono-meric and to lack a second actin-binding site outside the motor domain and so is not well suited to this role. Further, the F-actin that comprises the coats is highly dynamic and nucleated by the Cdc42-WASP-Arp2/3 pathway (Sokac et al., 2003). Thus, it is presumably comprised of branched networks with the plus ends of the filaments facing the membrane. We therefore suggest that *Xl*Myo1c works by linking dynamic actin to the membrane of CGs and so transduces the force provided by polymerizing filaments to compress the membrane.

Recent work on mammalian myosins-1c supports the idea that this motor could play such a role. First, to efficiently couple actin assembly to membrane compression, *Xl*Myo1c would need to be firmly anchored to the CG membrane; otherwise, its interaction with actively polymerizing actin might rip the myosin from the membrane surface. Consistent with this, the tail domain of mouse myosin-1c binds tightly and specifically to PIP_2-containing membranes (Hokanson and Ostap, 2006). Exocytosing CGs contain PIP_2 (Sokac and Bement, 2006), thus, the means for tight linkage between CG membranes and actin coats by *Xl*Myo1c is available in this system. Second, the ideal myosin transducer would entrain force production by the polymerizing actin filament to its own ATPase cycle. Consistent with this, release of ADP by rat myosin-1c is thought to be strain-dependent (Batters et al., 2004). Thus, myosins linked to an actively growing filament on CGs would preferentially move through the ATPase cycle as the filament pushed on the membrane and then rebind filaments near the membrane, in a rachet-like manner. Conversely, myosins linked to a nongrowing filament would preferentially hang on to the filament, ensuring some constant tethering between the membrane and assembling actin. Third, the optimal orientation for a motor that directs actin assembly-dependent force production on membrane compartments is parallel to the surface of the membrane compartment. Consistent with this, myosin-1c releases calmodulin from IQ domains upon calcium increase (Zhu et al., 1998), exposing other potential membrane-binding sites (Swanljung-Collins and Collins, 1992; Barylko et al., 2005; but see also Hokanson and Ostap, 2006). Thus, it is thought that under conditions of elevated calcium, the motor domain is oriented parallel to the membrane (Barylko et al., 2005).

How can the above model account for the finding that *Xl*Myo1c disruption results in increased actin assembly, as revealed by biochemical fractionation and increased numbers of actin comets? At least two, nonexclusive hypotheses suggest themselves. First, and most simply, by maintaining the plus ends of actin filaments in close contact with the membrane, *Xl*Myo1c might normally limit intercalation of actin monomer between the actin filament plus end and the membrane. Indeed, that immediate proximity to the membrane acts as a physical restraint on actin-filament growth is a basic assumption of a variety of models of actin-based cell locomotion (Mogilner and Oster, 1996; Alberts and Odell, 2004). Consequently, it is reasonable to imagine that increased distance between the filament plus

ends and the membrane would permit greater access of monomer to the plus ends and, thus, faster assembly. Second, *Xl*Myo1c might normally antagonize factors that bind to growing filaments and promote further filament nucleation or growth, such as the Arp2/3 complex or other myosins-1 that interact with CARMIL, a protein that binds to and inhibits capping protein (Yang et al., 2005).

Whether myosins-1 in other contexts can restrain actin assembly in vivo remains to be seen, but previous work is consistent with this possibility. Specifically, disruption of myosins-1 in *Dictyostelium* results in formation of ectopic pseudopodia (e.g., Titus et al., 1993). Similarly, acute disruption of mammalian myosin-1c in growth cones results in a rapid outgrowth of lamellapodia (Diefenbach et al., 2002).

Interestingly, the disruption of *Xl*Myo1c also impairs cortical contraction. The suppression of cortical contraction is unlikely to reflect a role for *Xl*Myo1c in powering this event, both for the reasons presented above for coat compression and because cortical contraction in eggs is myosin-2 dependent (Christensen et al., 1984). We instead suspect that the cortical contraction deficit either reflects improper anchorage of cortical F-actin to the PM or the inability of myosin-2 to efficiently utilize the ectopic F-actin resulting from *Xl*Myo1c disruption.

The effects of *Xl*Myo1c disruption on CG exocytosis are particularly fascinating given the previous report that expression of mammalian myosin-1c IQT in adipocytes suppresses exocytosis of the GLUT4 glucose transporter by an unknown mechanism (Bose et al., 2002). We can envision several possible explanations for inhibition of CG exocytosis. The first is that excess actin resulting from IQT expression provides a physical block to exocytosis, as observed in other systems (e.g., Muallem et al., 1995) and supported by our finding that cytochalasin treatment rescues the exocytosis defect. The second potential explanation is that IQT itself acts as a physical barrier to CG-PM fusion. However, constitutive exocytosis is unaffected by IQT expression at levels sufficient to completely suppress CG exocytosis, arguing against simple physical inhibition. A third possibility is that *Xl*Myo1c abets exocytosis by limiting actin assembly at the fusion pores and thus promoting their dilation. This idea is consistent with the observation that expression of IQT slows incorporation of dextran into exocytosing CGs and produces constricted fusion pore necks in these compartments. It is also consistent with the results of the cytochalasin rescue experiments. Of course, the above mechanisms are not mutually exclusive, and it is possible that each may contribute to the deficit in CG exocytosis.

Finally, in addition to demonstrating a key role for *Xl*Myo1c in egg activation, this study also provides a striking confirmation of the proposal that F-actin coats are responsible for retrieval of exocytosing CG membranes (Sokac et al., 2003). This point could not be directly tested before because inhibition of coat assembly by latrunculin treatment also results in immediate collapse of exocytosing CGs into the PM (Sokac et al., 2003). In contrast, disruption of *Xl*Myo1c does not result in collapse but does prevent coat compression. Consequently, the CG membranes are not retrieved and remain trapped beneath the PM. Because F-actin coats form in other eggs as well as in secretory cell types (reviewed in Sokac and Bement, 2006), it may be that myosin-1 similarly contributes to compartment retrieval following regulated exocytosis in a number of different systems.

Experimental Procedures

Degenerate PCR Screen

Degenerate primers ATP3 (5′-GGIGARWSIGGIGCIGGNAARAC-3′) and EAF-A (5′-GTYTTIGCRTTICCRAAIGCYTC-3′), corresponding to amino acids GESGAGKT and

EAFGNAKT, respectively, were used to amplify 12 different myosins from *Xenopus* ovary cDNA. Based on the closest vertebrate homolog identified by BLAST searching, these myosin fragments represent *Xl*Myo1b (100%, *Xt*Myo1b), *Xl*Myo1c (92%, *Rc*Myo1c), *Xl*Myo1d (100%, *Hs*Myo1D), *Xl*Myo1e (89%, *Hs*Myo1E), *Xl*Myo1f (100%, *Hs*Myo1F), *Xl*Myo2a (92%, *Hs*Myo2A), *Xl*Myo3 (67%, *Gg*Myo3), *Xl*Myo6 (100%, *Xt*Myo6), *Xl*Myo9a (100%, *Hs*Myo9A), *Xl*Myo9b (89%, *Hs*Myo9B), *Xl*Myo10 (70%, *Tn*Myo10), and *Xl*Myo18 (72%, *Tn*Myo18)where the percentage indicates percent amino acid identity, and initials indicate the following organisms: *Xt*, *Xenopus tropicalis*; *Rc*,*Rana catesbeiana*; *Hs*, *Homosapiens*;*Gg*, *Gallus gallus*; *Tn*, *Tetraodon nigroviridis*. Larger myosin fragments were then amplifiedwith upstream-specific primers for Myo1c (5′-CAGGTGGAGACCGTGAAA-3′), Myo1e (5′-GGAGGTGGCCCTAAAGTG-3′), Myo2a (5′-GCAACATCACACAAGTCT-3′), Myo9b (5′-TTGGGTGCTGGACCTGTA-3′), andMyo10 (5′-GAAAGCACCAAACTGCTG-3′), corresponding to amino acids QVETVK, GGGPKV, ATSHKS, ESTKLL, and LGAGPV, respectively, that were paired with downstream degenerate primers LDIY (5′-TCRAAICCRWADATRTCIAR-3′) or FEQF (5′-ARTT DATRCARAAYTGYTCRAA-3′), corresponding to amino acids LDIY/FGFE and FEQFCIN, respectively.

5′/3′ RACE and Morpholinos

For 5′ RACE, cDNA was made from egg poly(A)$^+$ RNA with a *Xl*Myo1c-specific primer (5′-GAGATAGTTTAGAATGTGACC-3′), corresponding to amino acids GHILNYL. For subsequent PCR, a nested *Xl*Myo1c primer (5′-GGATTGGACTGAAGAAGGCG-3′), corresponding to amino acids RLLQSN, was paired with a generic oligo-dT anchor primer (Roche Applied Biosciences, Indianapolis, IN). For 3′ RACE, two specific primers were designed against the *Xl*Myo1c 5′UTR (5′-CTGAGGAGTTGAGTGCTGTGAAGC-3′ and 5′-GTTGAGTGCTGTGAAGCTGAACAGG-3′) and used in sequential rounds of PCR. The morpholino (GeneTools; 5′-TTTTCCATGGTGACCCGGATCCCGA-3′) was designed against the *Xl*Myo1c 5′UTR; the control morpholino (5′-TTTACCATGGTCACGCGGTTCGCGA-3′) incorporated a five base pair mismatch.

RNA Isolation and Northern Blotting

Total RNA was extracted from staged oocytes and further fractionated to yield stage-specific poly(A)$^+$ RNA with the MicroPoly(A) Pure mRNA Isolation Kit (Ambion, Austin, TX). For developmental Northerns, poly(A)$^+$ RNA was quantified by spectrophotometry and equal quantities loaded per oogenic stage. For total versus poly(A)$^+$ RNA/stage 6 oocyte versus egg analysis, 30 oocyte/egg equivalents were loaded per lane. RNAs were blotted and processed according to Northern Max Blotting Kit (Ambion) specifications. Antisense RNA probes were transcribed in vitro, purified over G-50 spin columns, and labeled and detected with the Bright-Star Psoralen-Biotin Nonisotopic Labeling and Detection Kit (Ambion).

Protein Extraction and Immunoblotting

For stage 6 oocyte versus egg analysis of endogenous myosin or actin, 90 stage 6 oocytes or eggs were homogenized in 240 μl PHEME Buffer (60 mM K-PIPES, 25 mM HEPES, 10 mM EGTA, 2 mM $MgCl_2$ [pH 7.0] with KOH,1%Triton X-100, 5mMMgATP, 5 μg/ml leupeptin, 10 μg/ml aprotinin, 1 mM PefaBloc SC, 10 μg/ml chymostatin, 10 μg/ml pepstatin) with a mechanical homogenizer. Homogenates were spun at 14,000 × g, and the cytoplasmic layer collected and combined with sample buffer and then separated by SDS-PAGE. For cortical fractionations, single oocytes were disrupted in Solution A (250 mM sucrose, 10 mM HEPES, 1 mM EGTA, 2 mM $MgCl_2$ [pH 7.4] supplemented immediately before use with 1 mM PMSF, 1 μg/ml pepstatin A, 1 μg/ml leupeptin) by six to seven gentle passages through the orifice of a yellow pipet tip. Sample was spun at 720 × g for 3 min. Low-speed supernatant was collected and combined with sample buffer. Low-speed pellet

was re-extracted in Solution B (1% Triton X-100, 0.1 M NaCl, 50 mM Tris, 1 mM EDTA [pH 7.4]) by trituration through a yellow pipet tip. Sample was spun at 16,000 × g for 1 min. Supernatant was collected, combined with sample buffer, and subjected to SDS-PAGE.

For immunoblots primary antibodies anti-Myosin-1c (M2) (Wagner et al., 1992), anti-Myosin-2 (Biomedical Technologies, Stoughton, MA), and anti-actin (Amersham Biosciences) were used at a dilution of 1:500. Secondary antibodies anti-mouse IgG-HRP conjugate and anti-rabbit IgG-HRP conjugate (Promega, Madison, WI) were used at a dilution of 1:5000. Chemiluminescent detection proceeded according to standard ECL protocols.

Secretion Assays

For analysis of constitutive secretion, oocytes were injected with 10–50 ng of capped RNAs encoding GFP-rat syntaxin 1A (construct supplied by Dr. T. Coppola; Lausanne) or α1–β1 subunits (4:1 ratio) rat Na^+-K^+ ATPase (construct supplied by Dr. J.D. Horisberger; Lausanne) and incubated at 18°C for 48 hr. Cells were fractionated as above, and the fractions immunoblotted. Cortical granule secretion from single oocytes was monitored as previously described (Gundersen et al., 2002) following 30 min treatment with 1 μM PMA or 10 μM ionomycin at 20°C−22°C.

Capped RNA Synthesis

For expression of untagged or N-terminally eGFP-tagged *Xl*Myo1c constructs, myosin sequences were cloned into pCS^{2+} or custom vector pCS^{2+}eGFP, respectively. Transcription of capped RNA proceeded according to the SP6 or T7 mMessage mMachine High Yield Capped RNA Transcription Kit (Ambion) protocol with 1 μsg of template. RNA was extracted with an equal volume of phenol:chloroform (50:50). For rescue experiments, cells were injected with 80 ng HIQT and 40 ng IQT.

Cell Fixation and Staining

Egg activation was induced and proceeded for 2 min in 10 μM ionomycin (Calbiochem) in 1/10× OR2. The eGFP-*Xl*Myo1c-expressing oocytes, eggs, and activated eggs were fixed for 4 hr in 3.7% para-formaldehyde, 0.1% glutaraldehyde, and 0.4 units/ml Alexa568-phalloidin (Molecular Probes, Eugene, OR) in Myo1c Fix Buffer (10 mM HEPES, 10 mM EGTA, 100 mM KCl, 3 mM $MgCl_2$, 150 mM sucrose [pH 7.6]). Cells were bisected prior to staining with 1 unit/ml Alexa568-phalloidin for 12–14 hr. For immunofluorescence localization of *Xl*myo1c, activated eggs were fixed for 30 min in the presence of Alexa568 phalloidin, washed for 1 hr, bisected, and processed for immunofluorescence with a monoclonal anti-myosin-1c antibody (Wagner et al., 1992).

Microscopy and Image Analysis

Oocytes and eggs were prepared, injected, cultured, and mounted as previously described (Sokac et al., 2003). Imaging was performed with a Zeiss Axiovert 100 M microscope (Carl Zeiss, Inc., Thornwood, NY) with Bio-Rad 1024 × 1024 Lasersharp Confocal Software (Bio-Rad Laboratories, Hercules, CA) with a numerical aperture 1.4, 63× objective lens. For quantification of fluorescence intensities, the NIH Object-Image v2.06 software was used. Z series and time-lapse, single optical plane movies and 4D renderings were generated with Volocity v10 software (Improvision, Lexington, MA). All other image processing was done with Adobe Photoshop 7.0 (Adobe Systems).

Supplementary Material

Refer to Web version on PubMed Central for supplementary material.

Acknowledgments

This work was supported by the National Institutes of Health via grants to W.M.B. (GM052932-06) and C.B.G. (MH59938). Many thanks to Mark Wagner (Indiana University) for providing the myosin-1c antibody.

References

Alberts JB, Odell GM. In silico reconstitution of *Listeria* propulsion exhibits nano-saltation. PLoS Biol 2004;2:2054–2066.

2. Barylko B, Jung G, Albanesi JP. Structure, function, and regulation of myosin-1c. Acta Biochim. Pol 2005;52:373–380. [PubMed: 15933767]

Batters C, Arthur CP, Lin A, Porter J, Geeves MA, Milligan RA, Molloy JE, Coluccio LM. Myo1c is designed for the adaptation response in the inner ear. EMBO J 2004;23:1433–1440. [PubMed: 15014434]

Bement WM, Hasson T, Wirth JA, Cheney RE, Mooseker MS. Identification and overlapping expression of multiple unconventional myosin genes in vertebrate cell types. Proc. Natl. Acad. Sci. USA 1994;91:6549–6553. [PubMed: 8022818]

Bose A, Guilherme A, Robida SI, Nicoloro SM, Zhou QL, Jiang ZY, Pomerleau DP, Czech MP. Glucose transporter recycling in response to insulin is facilitated by myosin Myo1c. Nature 2002;420:821–824. [PubMed: 12490950]

Christensen K, Sauterer R, Merriam RW. Role of soluble myosin in cortical contractions of *Xenopus* eggs. Nature 1984;310:150–151. [PubMed: 6738711]

Colman A, Morser J, Lane C, Besley J, Wylie C, Valle G. Fate of secretory proteins trapped in oocytes of *Xenopus laevis* by disruption of the cytoskeleton or by imbalanced subunit synthesis. J. Cell Biol 1981;91:770–780. [PubMed: 6173386]

Coluccio LM. Myosin I. Am. J. Physiol 1997;273:C347–C359. [PubMed: 9277333]

Diefenbach TJ, Latham VM, Yimlamai D, Liu CA, Herman IM, Jay DG. Myosin 1c and myosin IIB serve opposing roles in lamellipodial dynamics of the neuronal growth cone. J. Cell Biol 2002;158:1207–1217. [PubMed: 12356865]

Doberstein SK, Baines IC, Wiegand G, Korn ED, Pollard TD. Inhibition of contractile vacuole function in vivo by antibodies against myosin-I. Nature 1993;365:841–843. [PubMed: 8413668]

Elinson RP. Fertilization of immature frog eggs: cleavage and development following subsequent activation. J. Embryol. Exp. Morphol 1977;37:187–201. [PubMed: 300772]

Gard DL, Cha BJ, Roeder AD. F-actin is required for spindle anchoring and rotation in *Xenopus* oocytes: a re-examination of the effects of cytochalasin B on oocyte maturation. Zygote 1995;3:17–26. [PubMed: 7613871]

Gray NK, Wickens M. Control of translation initiation in animals. Annu. Rev. Cell Dev. Biol 1998;14:399–458. [PubMed: 9891789]

Gundersen CB, Kohan SA, Chen Q, Iagnemma J, Umbach JA. Activation of protein kinase Ceta triggers cortical granule exocytosis in *Xenopus* oocytes. J. Cell Sci 2002;115:1313–1320. [PubMed: 11884530]

Heasman J, Kofron M, Wylie C. Beta-catenin signaling activity dissected in the early Xenopus embryo: a novel antisense approach. Dev. Biol 2000;222:124–134. [PubMed: 10885751]

Hokanson DE, Ostap EM. Myo1c binds tightly and specifically to phosphatidylinositol 4,5-bisphosphate and inositol 1,4,5-trisphosphate. Proc. Natl. Acad. Sci. USA 2006;103:3118–3123. [PubMed: 16492791]

Liu C, Smith LD. Differential accumulation of mRNA and interspersed RNA during *Xenopus* oogenesis and embryogenesis. Zygote 1994;2:307–316. [PubMed: 8665161]

Mogilner A, Oster G. Cell motility driven by actin polymerization. Biophys. J 1996;71:3030–3045. [PubMed: 8968574]

Muallem S, Kwiatkowska K, Xu X, Yin HL. Actin filament disassembly is a sufficient final trigger for exocytosis in non-excitable cells. J. Cell Biol 1995;128:589–598. [PubMed: 7860632]

Reizes O, Barylko B, Li C, Sudhof TC, Albanesi JP. Domain structure of a mammalian myosin I beta. Proc. Natl. Acad. Sci. USA 1994;91:6349–6353. [PubMed: 8022785]

Robbie EP, Peterson M, Amaya E, Musci TJ. Temporal regulation of the *Xenopus* FGF receptor in development: a translation inhibitory element in the 3′ untranslated region. Development 1995;121:1775–1785. [PubMed: 7600993]

Sheets MD, Fox CA, Hunt T, Vande Woude G, Wickens M. The 3′-untranslated regions of c-mos and cyclin mRNAs stimulate translation by regulating cytoplasmic polyadenylation. Genes Dev 1994;8:926–938. [PubMed: 7926777]

Sokac AM, Bement WM. Regulation and expression of metazoan unconventional myosins. Int. Rev. Cytol 2000;200:197–304. [PubMed: 10965469]

Sokac AM, Bement WM. Kiss-and-coat and compartment mixing: coupling exocytosis to signal generation and local actin assembly. Mol. Biol. Cell 2006;17:1495–1502. [PubMed: 16436510]

Sokac AM, Co C, Taunton J, Bement W. Cdc42-dependent actin polymerization during compensatory endocytosis in *Xenopus* eggs. Nat. Cell Biol 2003;5:727–732. [PubMed: 12872130]

Soldati T. Unconventional myosins, actin dynamics and endocytosis: a menage a trois? Traffic 2003;4:358–366. [PubMed: 12753645]

Sun Y, Martin AC, Drubin DG. Endocytic internalization in budding yeast requires coordinated actin nucleation and Myosin motor activity. Dev. Cell 2006;11:33–46. [PubMed: 16824951]

Swanljung-Collins H, Collins JH. Phosphorylation of brush border myosin I by protein kinase C is regulated by $Ca^{(2+)}$-stimulated binding of myosin I to phosphatidylserine concerted with calmodulin dissociation. J. Biol. Chem 1992;267:3445–3454. [PubMed: 1737797]

Tang N, Lin T, Ostap EM. Dynamics of Myo1c (myosin-Ibeta) lipid binding and dissociation. J. Biol. Chem 2002;277:42763–42768. [PubMed: 12221091]

Taunton J, Rowning BA, Coughlin ML, Wu M, Moon RT, Mitchison TJ, Larabell CA. Actin-dependent propulsion of endosomes and lysosomes by recruitment of N-WASP. J. Cell Biol 2000;148:519–530. [PubMed: 10662777]

Titus MA, Wessels D, Spudich JA, Soll D. The unconventional myosin encoded by the myoA gene plays a role in *Dictyostelium* motility. Mol. Biol. Cell 1993;4:233–246. [PubMed: 8382977]

Wagner MC, Barylko B, Albanesi JP. Tissue distribution and subcellular localization of mammalian myosin I. J. Cell Biol 1992;119:163–170. [PubMed: 1527166]

Welch MD, Mullins RD. Cellular control of actin nucleation. Annu. Rev. Cell Dev. Biol 2002;18:247–288. [PubMed: 12142287]

Wolf DP. The cortical granule reaction in living eggs of the toad, *Xenopus laevis*. Dev. Biol 1974;36:62–71. [PubMed: 4822840]

Yang C, Pring M, Wear MA, Huang M, Cooper JA, Svitkina TM, Zigmond SH. Mammalian CARMIL inhibits actin filament capping by capping protein. Dev. Cell 2005;9:209–221. [PubMed: 16054028]

Yumura S, Uyeda TQ. Myosins and cell dynamics in cellular slime molds. Int. Rev. Cytol 2003;224:173–225. [PubMed: 12722951]

Zhu T, Beckingham K, Ikebe M. High affinity Ca^{2+} binding sites of calmodulin are critical for the regulation of myosin Ibeta motor function. J. Biol. Chem 1998;273:20481–20486. [PubMed: 9685403]

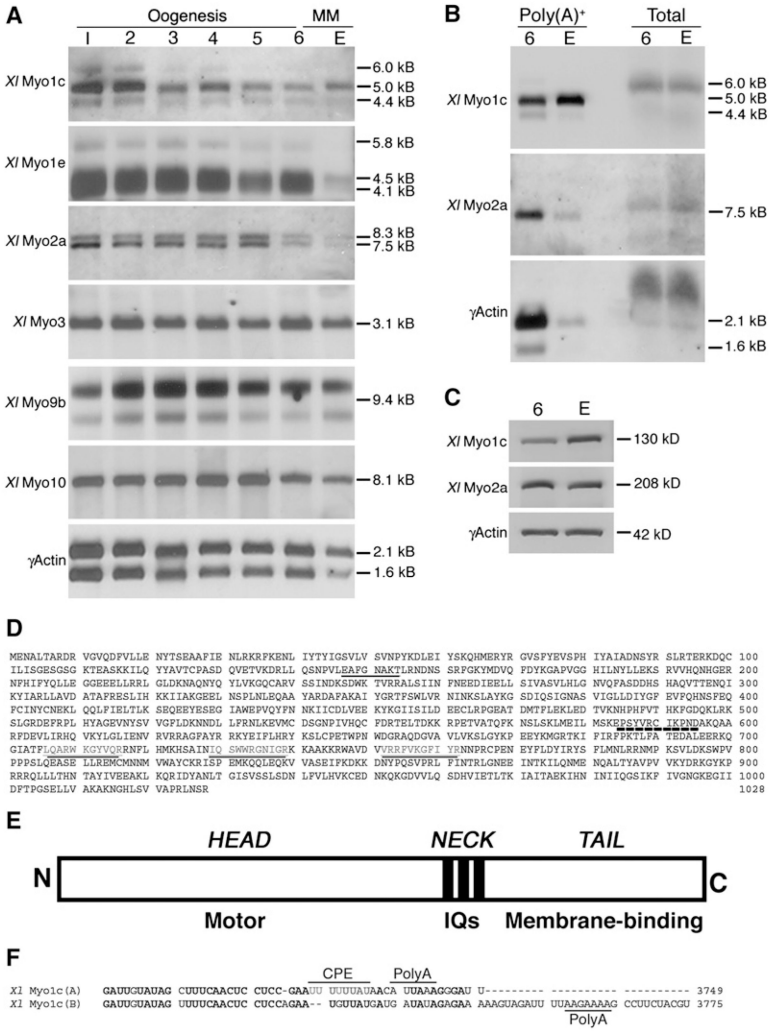

Figure 1. *Xl*Myo1c Is Specifically Upregulated by Polyadenylation during Meiotic Maturation

(A) Poly(A)$^+$ northern blots of six myosins and γ-actin from the six stages of oogenesis (1–6; "Oogenesis") and the egg following meiotic maturation (E; "MM"). Levels of *Xl*Myo1c Poly(A)$^+$ RNA increase during meiotic maturation, while levels for all of the other myosins and γ-actin sharply decrease during the same interval (compare 6 to E). Equal amounts of RNA were loaded in each lane.

(B) Poly(A)$^+$ and total RNA before (6) and after (E) meiotic maturation for *Xl*Myo1c, *Xl*Myo2a, and γ-actin. Total RNA levels do not change for any message, while poly(A)$^+$ levels drop sharply for *Xl*Myo2a and γ-actin. In contrast, poly(A)$^+$ levels increase for *Xl*Myo1c. Thirty oocyte equivalents of RNA were loaded for each lane.

(C) Immunoblot comparison of protein levels before (6) and after (E) meiotic maturation for *Xl*Myo1c, *Xl*Myo2a, and γ-actin. *Xl*Myo1c levels increase during meiotic maturation, while those of *Xl*Myo2a and γ-actin do not.

(D) The complete coding sequence for *Xl*Myo1c. The ATP-binding region (dark underline) and actin-binding region (dashed underline) are indicated, as are the three IQ motifs (dark underline, gray text).

(E) Schematic diagram of *Xl*Myo1c.

(F) Alternative 3′UTRs for *Xl*Myo1c. Both 3′UTRs include nuclear polyadenylation signals (PolyA) but only *Xl*Myo1c(A) has the cytoplasmic polyadenylation element (CPE) necessary to direct polyadenylation during meiotic maturation.

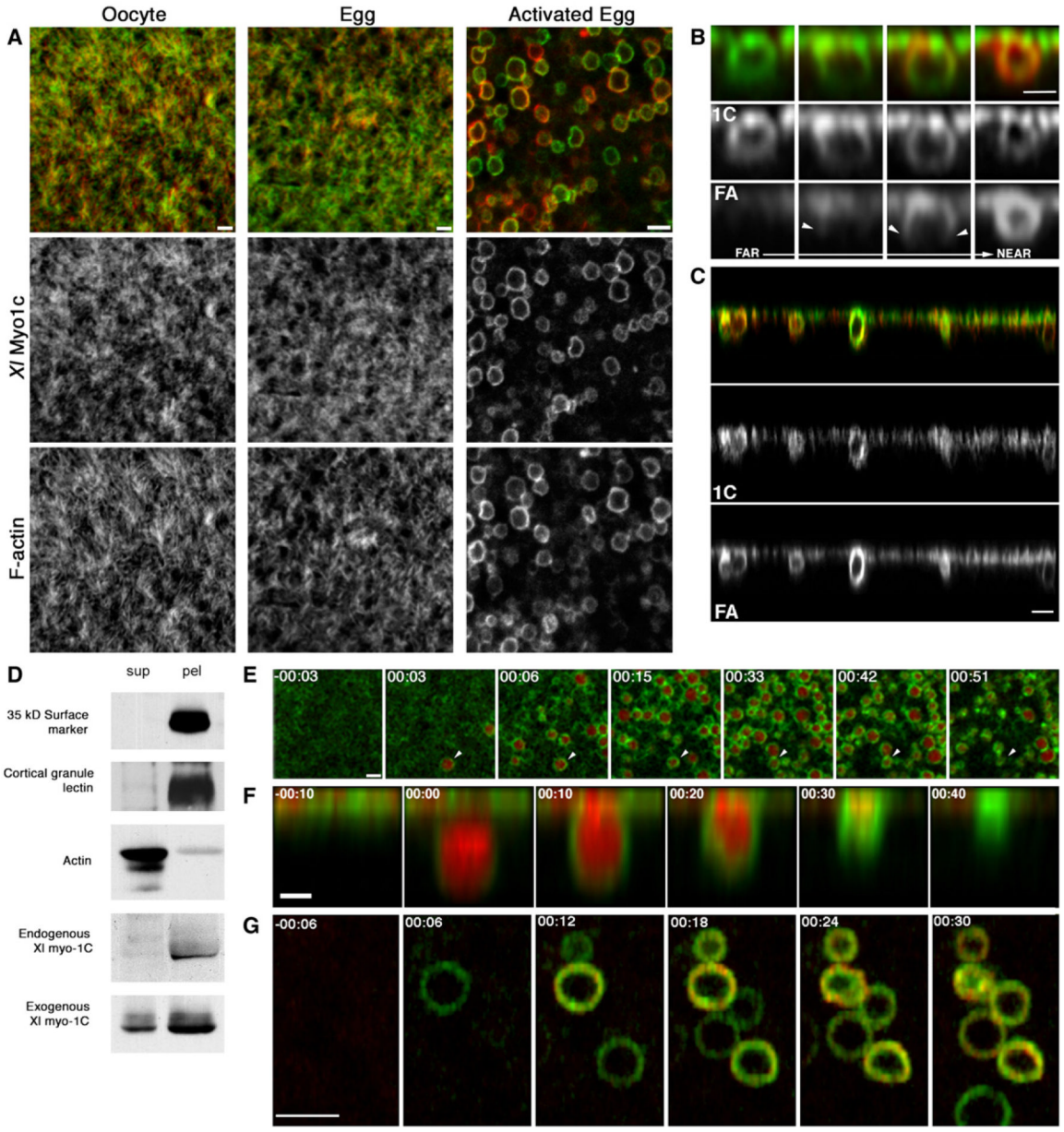

Figure 2. *Xl*Myo1c Is Recruited to Exocytosing CGs upon Egg Activation

(A) Single plane images of eGFP-*Xl*Myo1c (green) and F-actin (red) in oocytes, eggs, and activated eggs. Surface views show *Xl*Myo1c at the PM overlying F-actin microvilli. Upon egg activation, views just below the PM show *Xl*Myo1c is recruited to exocytosing CGs, along with actin.

(B) Z sections of a prick-activated egg. In regions far from the prick site, *Xl*Myo1c completely surrounds CGs that do not yet have actin coats. At intermediate distances from the prick site, exocytosing CGs are partially enclosed by actin coats (arrowheads). Near the prick site, exocytosing CGs are completely enclosed by actin coats.

(C) Z sections of endogenous *Xl*Myo1c (red; 1C) and F-actin (green; FA) in activated eggs. *Xl*Myo1c localizes to the PM and exocytosing CGs.

(D) Immunoblot analysis of cortical (pel) and cytoplasmic (sup) fractions from *Xenopus* oocytes. Cortical fractions are enriched in cell-surface proteins and CG lectins, while most

of the actin is cytoplasmic. Both endogenous and exogenous *Xl*Myo1c are enriched in the cortical fraction.

(E) Time-lapse images from a single plane just beneath the PM, showing eGFP-*Xl*Myo1c (green) before and after egg activation by IP_3 uncaging in the presence of extracellular TR-dextran (red) to reveal exocytosing CGs. Within 3 s of uncaging, CGs exocytose (arrowhead), become surrounded by eGFP-*Xl*Myo1c, and are then compressed. See Movie S1.

(F) Z section, time-lapse images of eGFP-*Xl*Myo1c recruitment to exocytosing CGs that are then compressed.

(G) Single plane time-lapse images showing eGFP-*Xl*Myo1c (green) and actin (red) before and after activation by IP_3 uncaging. eGFP-*Xl*Myo1c is recruited before actin. Time is in min:sec; bars are 5 μm.

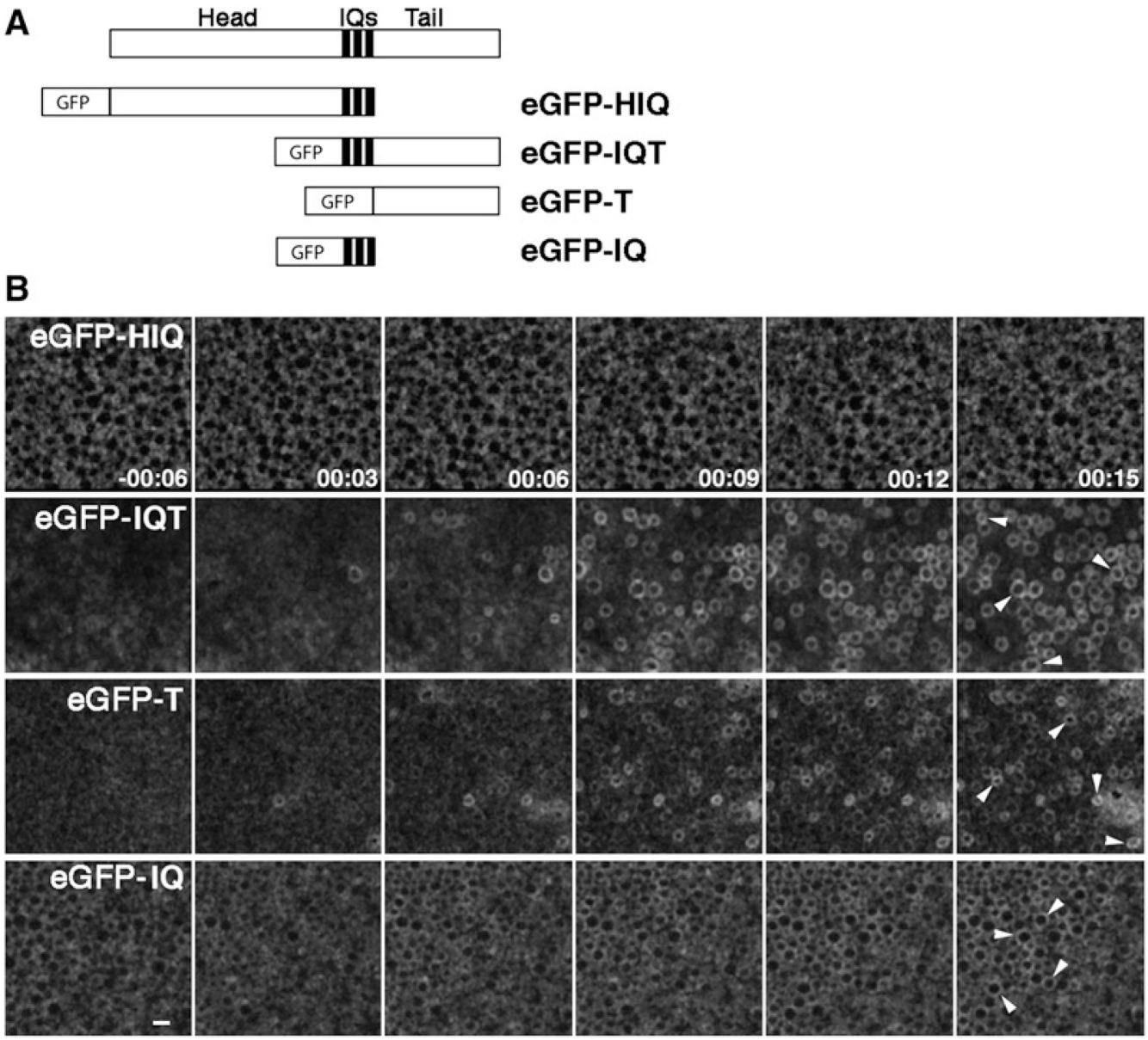

Figure 3. Neck and Tail Constructs of *Xl*Myo1c Are Recruited to Exocytosing CGs

(A) Schematic diagram of eGFP-tagged *Xl*Myo1c constructs.

(B) Time-lapse images, from a single plane just below the PM, showing eGFP-HIQ, eGFP-IQT, eGFP-T, and eGFP-IQ before and after egg activation by IP_3 uncaging. While eGFP-HIQ remains cytoplasmic following activation, eGFP-IQT, eGFP-T, and eGFP-IQ are recruited to exocytosing CGs (arrowheads). Time is in min:sec; bar is 5 μm.

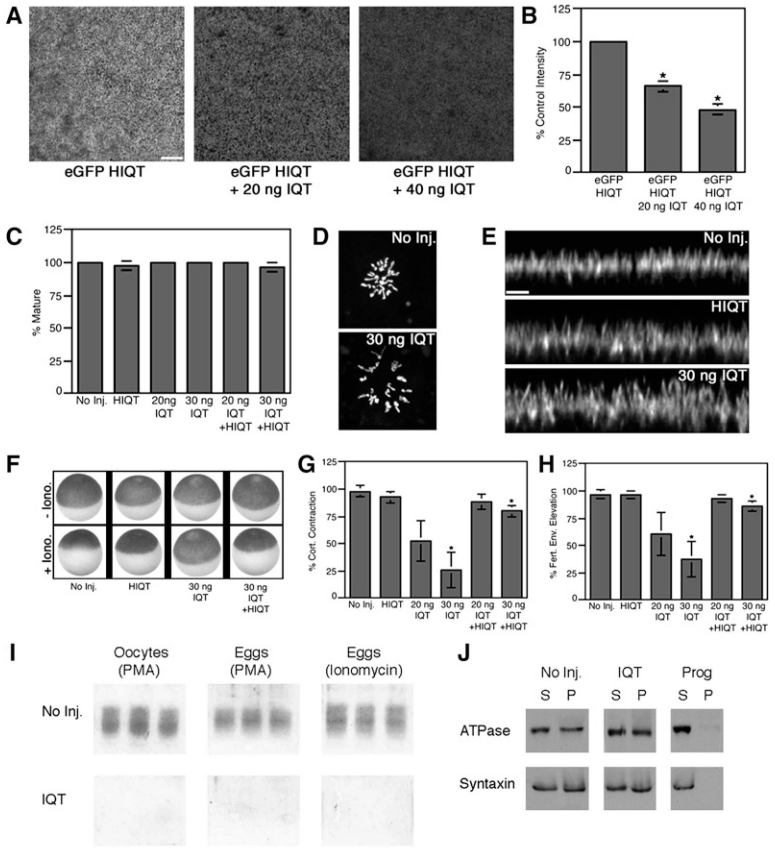

Figure 4. *Xl*Myo1c Disruption by Dominant-Negative IQT Expression Perturbs Actin/Membrane Events of Egg Activation

(A) Single plane images of eGFP-HIQT signal at the PM showing fluorescence decreases with increasing amounts of IQT coexpression.

(B) Quantification of decreasing eGFP-HIQT signal at the PM with coexpression of IQT. Results are mean ± SEM; n = 3 independent experiments. Asterisks indicate $p < 0.05$.

(C) Quantification of oocytes that mature to eggs following progesterone treatment. Expression of IQT has no effect on meiotic maturation relative to controls.

(D) Images of propidium-iodide-stained meiotic spindle chromosomes show that IQT expression does not impair spindle rotation during meiotic maturation in that chromosomes are found in classic rosette patterns, parallel to the PM.

(E) Z sections of PM showing F-actin in microvilli. IQT expression results in microvilli that are longer than in control cells.

(F) Images showing that IQT suppresses cortical contraction in eggs. Calcium ionophore (+Iono.) triggers movement of pigment to animal pole in uninjected (No inj.) and HIQT-injected cells but not in IQT-injected cells. Coexpression of HIQT rescues the effects of IQT.

(G) Quantification of cortical contraction in eggs. The effects of IQT are dose dependent and are rescued by coexpression of HIQT. Results are mean ± SEM; n = 3 independent experiments. Asterisks indicate $p < 0.05$.

(H) Quantification of oocytes with fertilization envelopes 2 min after calcium ionophore treatment. IQT expression slows exocytosis in a dose-dependent manner, and this slowing is rescued by coexpression of HIQT. Results are mean ± SEM, n = 3 independent experiments. Asterisks indicate $p < 0.05$.

(I) Coomassie-stained gels showing 2 day expression of IQT completely suppresses CG exocytosis in oocytes treated with PMA or eggs treated with PMA or calcium ionophore. Each lane represents CG lectin released from a single oocyte in uninjected (No inj.) and IQT-injected (IQT) cells.
(J) Immunoblots of cortical (P) and cytoplasmic (S) fractions showing IQT does not inhibit constitutive exocytosis of Na^+-K^+ ATPase or syntaxin-1. While IQT had no effect on exocytosis of these proteins at the PM relative to uninjected controls, progesterone treatment sharply suppressed their exocytosis.

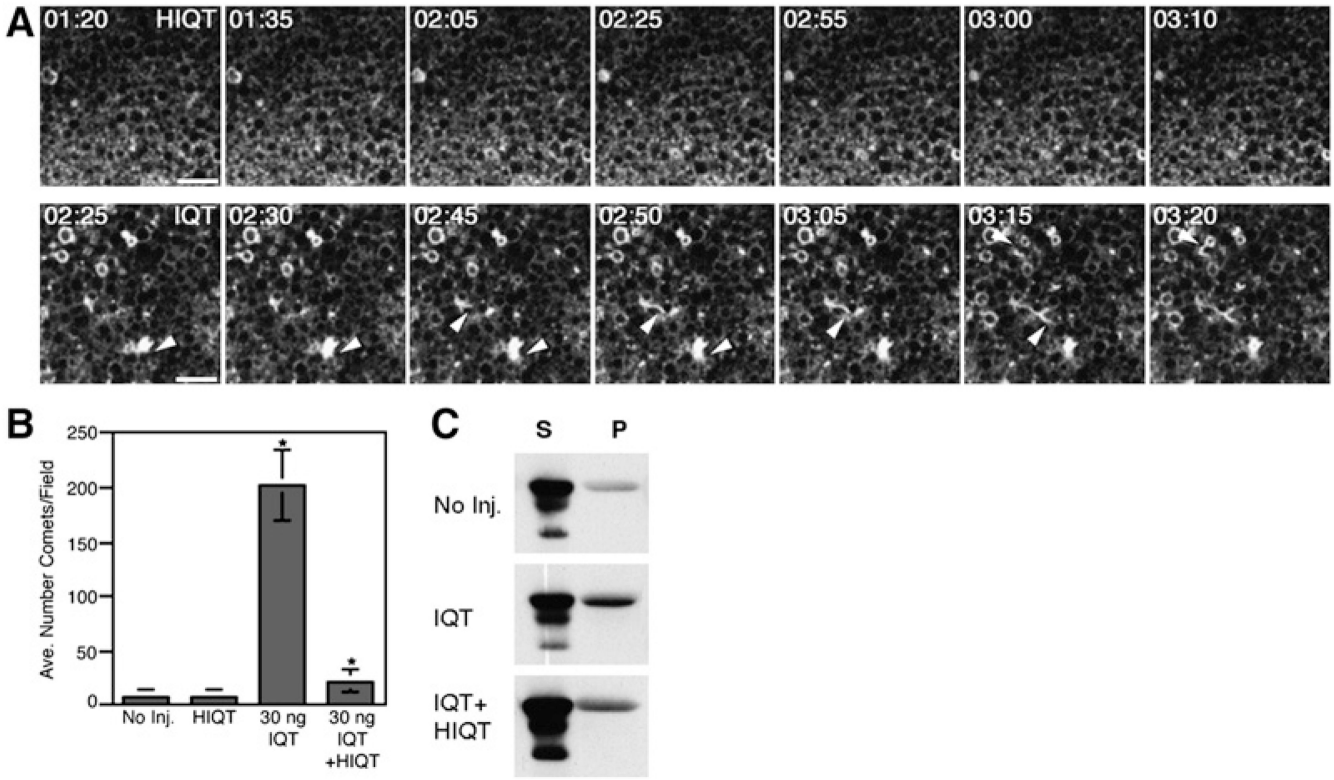

Figure 5. *Xl*Myo1c Disruption by Dominant-Negative IQT Expression Leads to Unrestrained Actin Assembly

(A) Single plane time-lapse images of oocytes injected with either HIQT or IQT and Alexa488-G-actin and then treated with PMA. F-actin comets (arrowheads) are numerous in the IQT but not the HIQT-expressing oocytes.

(B) Quantification of the average number of comets appearing in PMA-treated oocytes. IQT significantly increases comet number relative to controls, while coexpression of IQT with HIQT sharply reduces this effect. Results are mean ± SEM; n = 3 independent experiments. Asterisk indicates $p < 0.05$.

(C) Immunoblot of actin in cortical (P) and cytoplasmic (S) fractions shows that IQT increases levels of actin associated with the cortical fraction. This effect is rescued by coexpression of IQT with HIQT. Bars are 10 μm.

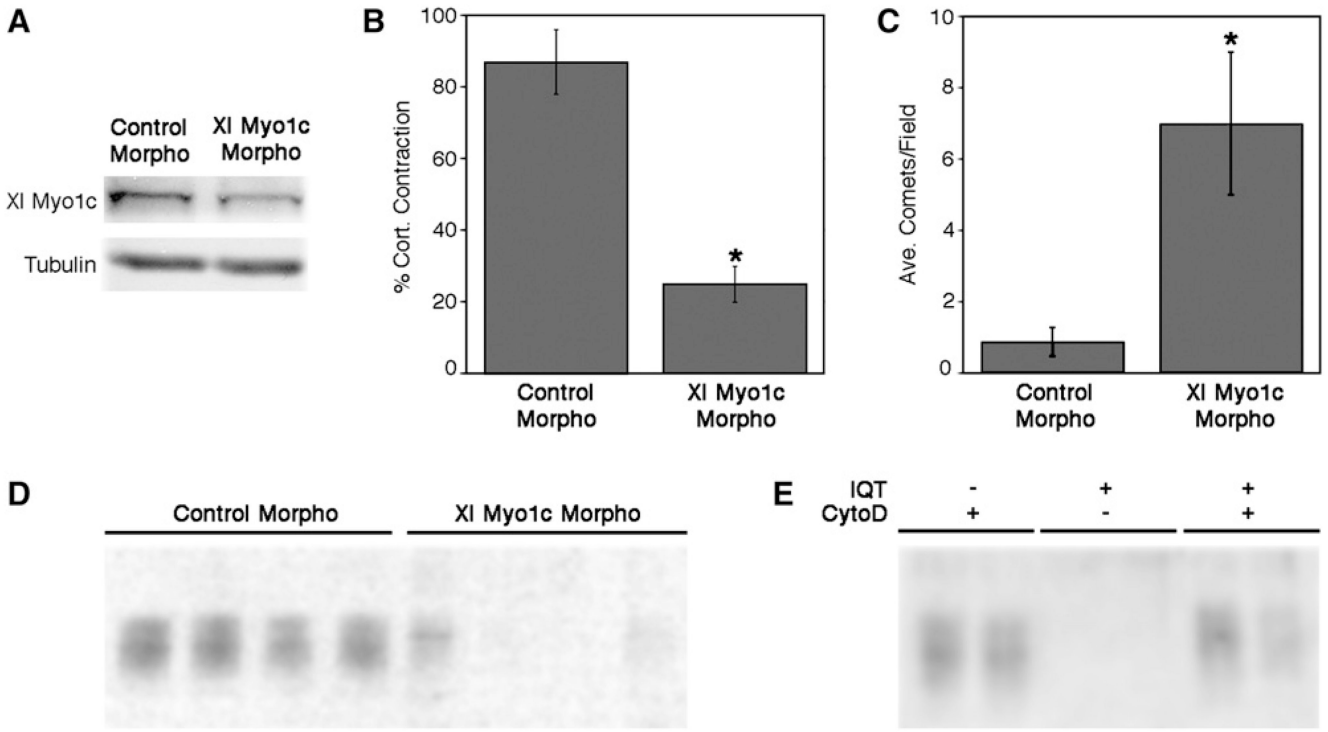

Figure 6. *Xl*Myo1c Disruption by a Morpholino Perturbs Actin/Membrane Events of Egg Activation

(A) Immunoblot showing a *Xl*Myo1c morpholino (Xl Myo1c Morpho) prevents the increase in *Xl*Myo1c protein during meiotic maturation, but the mismatch control morpholino (Control Morpho) does not. Tubulin was probed as a loading control.

(B) Quantification of cortical contraction in eggs with *Xl*Myo1c morpholino or control morpholino. The *Xl*Myo1c morpholino suppresses cortical contraction. Results are mean ± SEM; n = 3 independent experiments. Asterisk indicates $p < 0.05$.

(C) Quantification of actin comets in oocytes with *Xl*Myo1c morpholino or control morpholino. *Xl*Myo1c morpholino causes a significant increase in actin comets in oocytes. Results are mean ± SEM; n = 3 independent experiments. Asterisk indicates $p < 0.05$.

(D) Coomassie-stained gel showing the *Xl*Myo1c morpholino sharply reduces CG exocytosis in eggs.

(E) Coomassie-stained gel showing that cytochalasin D (CytoD) rescues CG exocytosis in IQT-expressing cells (IQT).

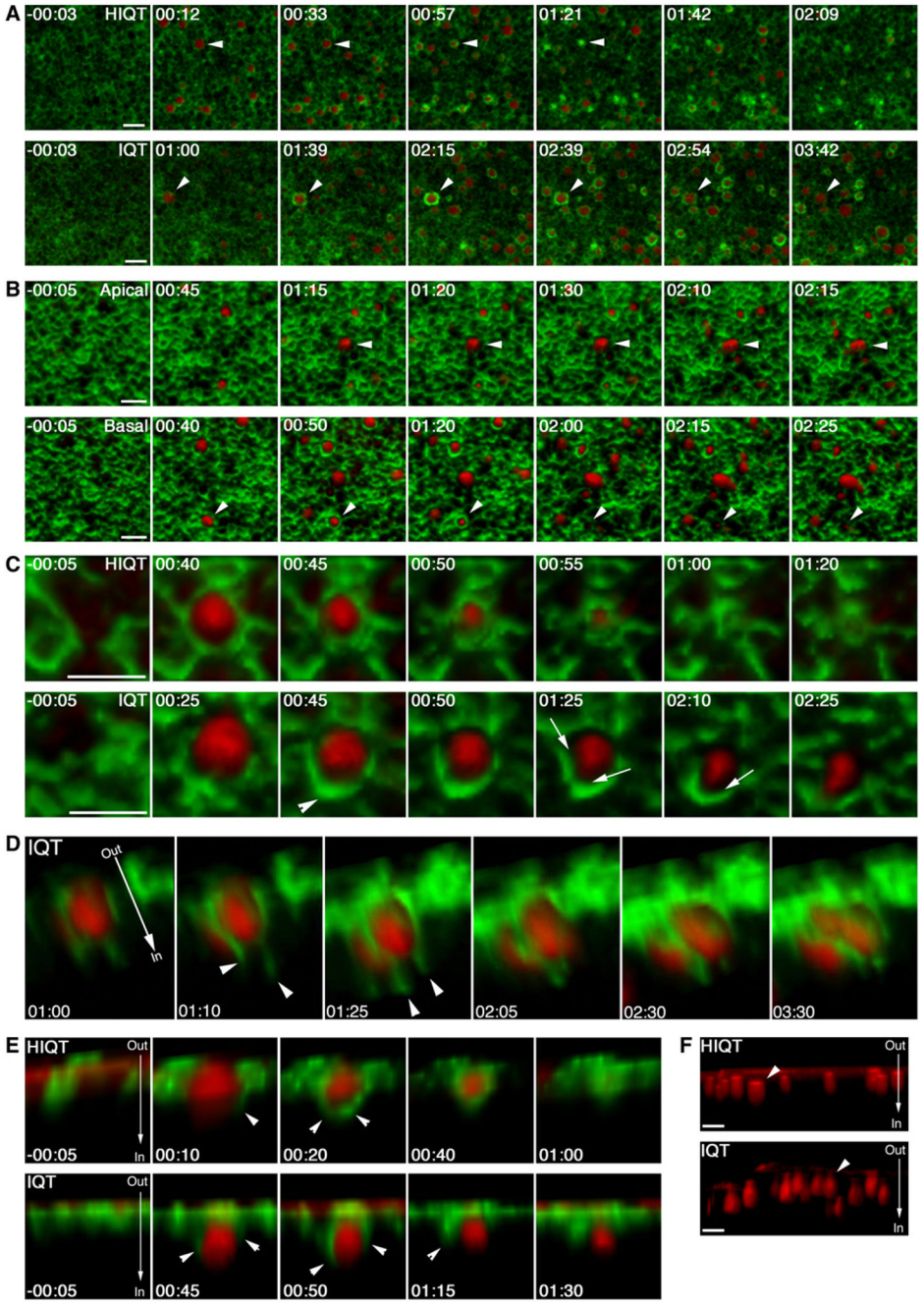

Figure 7. *Xl*Myo1c Couples Dynamic Actin to Exocytosing CG Membranes

(A) Time-lapse images from a single plane just below the PM of Alexa488-G-actin (green) in eggs expressing either HIQT or IQT. Eggs were activated by IP_3 uncaging in the presence of extracellular TR-dextran (red) to reveal exocytosing CGs. In HIQT eggs, actin coats rapidly enclose and compress exocytosing CGs (arrowheads). See Movie S2. In IQT eggs, CG exocytosis is slower, as judged by delay in the appearance of dextran. Also, actin coats assemble around exocytosing CGs but fail to compress and eventually dissipate (arrowheads). See Movie S3.

(B) Low magnification, 4D time-lapse images of eggs expressing IQT. Uncaging triggers exocytosis; however, CGs are not covered over by actin coats on either the exoplasmic

surface (Apical) or the cytoplasmic surface (Basal). See Movie S4 (Apical) and Movie S5 (Basal).

(C) High magnification, 4D time-lapse images of eggs expressing either HIQT or IQT. In HIQT eggs, basal views show that the actin coat tracks closely over the cytoplasmic surface of the exocytosing CG, eventually enclosing it. See Movie S6. In IQT eggs, basal views show that the actin coat forms (arrowhead) but is separated from the cytoplasmic surface of the CG (arrows). The coat eventually regresses. See Movie S7.

(D) High magnification, 4D time-lapse images of an egg expressing IQT. This tilted z view shows perturbed actin-coat assembly in the form of actin fingers (arrowheads) that partially track along the CG but then extend into the cytoplasm. The fingers grow and shrink over time, but the CG is never completely surrounded by an actin coat. Compression of the incomplete coat causes the CG to squirt out through a region with no coat. (“Out” and “In” indicate the outside and the inside of the cell, respectively.) See Movie S8.

(E) High magnification, 4D time-lapse images of eggs expressing either HIQT or IQT. Z views show in HIQT eggs, actin coats extend downward from the PM (arrowheads), enclose the exocytosing CG, and compress upward. See Movie S9. In IQT eggs, while coats start to assemble downward from the PM (arrowheads), they subsequently regress upwards. See Movie S10.

(F) Z views from eggs expressing either HIQT or IQT. Only the TR-dextran is shown. In HIQT eggs, exocytosing CGs have broad necks where they fuse to the PM (arrowhead). In IQT eggs, the necks are narrow. Time is in min:sec; bars are 5 μm.